PROCEEDINGS, 48th Workshop on Geothermal Reservoir Engineering
Stanford University, Stanford, California, February 6-8, 2023
SGP-TR-224

The 2022 WHOLESCALE deployment at San Emidio, Nevada, U.S.

Kurt L. Feigl, Hao Guo (1), Erin Cunningham (1), Jesse Hampton (1), Matthew Folsom (2), John Akerley(2), Matteo Cusini (3), Chris Sherman (3), Ian Warren (5), Corné Kreemer (4), Hiroki Sone (1) Michael A. Cardiff (1), Neal E. Lord(1), Peter E. Sobol (1), Sam A. Batzli (1), Clifford H. Thurber (1), and Herbert F. Wang (1)

(1) University of Wisconsin-Madison, Madison, WI, United States;
(2) Ormat Technologies Inc., Reno, NV, United States;
(3) Lawrence Livermore National Laboratory, Livermore, CA, United States;
(4) University of Nevada Reno, NV, United States;
(5) National Renewable Energy Lab. (NREL), Golden, CO, United States

feigl@wisc.edu

ABSTRACT

The WHOLESCALE acronym stands for Water & Hole Observations Leverage Effective Stress Calculations and Lessen Expenses. The goal of the WHOLESCALE project is to simulate the spatial distribution and temporal evolution of stress in the geothermal system at San Emidio in Nevada, United States. To reach this goal, the WHOLESCALE team is developing a methodology that will incorporate and interpret data from four methods of measurement into a multi-physics model that couples thermal, hydrological, and mechanical (T-H-M) processes over spatial scales ranging from the diameter of a borehole (~0.1 m) to the extent of the entire field (~10 km) and temporal scales ranging from the duration of a microseismic event (~1 second) to the typical lifetime of a producing field (3 decades). The study site at San Emidio includes a volume with length of ~6 km, width ~5 km, and depth ~2 km.

The WHOLESCALE team is taking advantage of the perturbations created by changes in pumping operations during planned shutdowns in 2016, 2021, and 2022 to infer temporal changes in the state of stress in the geothermal system. This rheological experiment is based on the key idea that increasing pore-fluid pressure reduces the effective normal stress acting across preexisting faults. The WHOLESCALE team conducted a field experiment in 2022 to collect data from seismology, drilling, geology, geodesy, and hydrology.

In this paper, we provide a snapshot of work in progress.

The work presented herein has been funded in part by the Office of Energy Efficiency and Renewable Energy (EERE), U.S. Department of Energy, under Award Number DE-EE0009032.

Keywords: WHOLESCALE, San Emidio, EGS, GPS, INSAR, FEM

INTRODUCTION

The San Emidio geothermal area is located ~100 km north of Reno Nevada in the northwestern Basin and Range province, as described previously [*Lund and Lienau*, 1994; *Matlick*, 1995; *Rhodes et al.*, 2010; *Warren*, 2010; *Eneva et al.*, 2011; *Moeck*, 2011; *Rhodes*, 2011; *Rhodes et al.*, 2011; *Faulds*, 2014; *UNR*, 2014; *Reinisch et al.*, 2019; *Feigl et al.*, 2020; *Folsom et al.*, 2020; *Folsom et al.*, 2021; *Thurber et al.*, 2021a; *Thurber et al.*, 2021b; *Feigl et al.*, 2022; *Guo et al.*, 2022; *Jahnke et al.*, 2022; *Sone et al.*, 2023; *Jahnke et al.*, in review].

The San Emidio geothermal system occupies a right step in a North-striking, West-dipping, normal fault zone. Minor dilation and high fault density within the right step likely produce the permeability necessary for deep fluid circulation [*Eneva et al.*, 2011]. Power was first produced in 1987 with a 3.6-MW binary plant, and average production increased to 9 MW (net) following commissioning of a new power plant in 2012. Production has ranged from less than 190 L/s to more than 280 L/s at temperatures of 140–148˚C. Drilling, geological, geophysical, and geochemical data sets collected since the 1970s help constrain controls on the geothermal resource and the structural setting (Figure 1 and Figure 2).

The geothermal field at San Emidio provides an ideal laboratory for understanding subsurface stress. The data collected over more than 20 years of operating experience characterize the structure, temperature, microseismicity, and permeability, all of which are directly associated with changes in the stress within the geothermal system. The data sets include historic drilling records, magnetotelluric resistivity, seismic reflection imaging, passive seismic emission tomography (PSET), microseismicity analysis, and gravimetric surveys.

Our WHOLESCALE team includes researchers at two universities and two national laboratories working in a public-private partnership with Ormat Technologies Inc. The WHOLESCALE project is funded by a peer-reviewed grant awarded by the Geothermal Technologies Office of the U.S. Department of Energy. The goal of the WHOLESCALE project is to simulate the spatial distribution and temporal evolution of stress in a geothermal system. To reach this goal, the WHOLESCALE team is developing a methodology to incorporate and interpret data from multiple methods of measurement into a multi-physics model that couples thermal, hydrological, and mechanical (T-H-M) processes over spatial scales ranging from the diameter of a borehole (~0.1 m) to the extent of the entire field (~10 km) and temporal scales ranging from the duration of a microseismic event (~1 second) to the typical lifetime of a producing field (3 decades).

Understanding subsurface stress can aid the development, drilling, and operational phases of geothermal operations. In this paper, we focus on the temporal changes in stress manifested by seismicity. Operators need a methodology to predict how these changes occur in time and space to manage the resource over the long term. The state of stress changes as a highly nonlinear response to multiple physical processes that can only be tracked by modern computational analysis. Accordingly, our methodology is an integrated geophysical and numerical approach for predicting the stress in a geothermal system. In short, "if we can model it, we can manage it".

DATA AND METHODS

The WHOLESCALE team is taking advantage of the perturbations created by pumping operations to infer temporal changes in the state of stress in the geothermal system. This rheological experiment is based on the key idea that increasing pore-fluid pressure reduces the effective normal stress acting across preexisting faults. Accordingly, the WHOLESCALE team is analyzing multiple types of observational data at San Emidio, measuring material properties of San Emidio rock samples in our laboratory, and performing simultations with a multiphysics T-H-M modeling code named GEOSX that has been developed at Lawrence Livermore National Laboratory.

Geology

An updated 3-dimensional geologic and structural model of San Emidio has been completed, following an exhaustive review and re-interpretation of well cuttings and logs. The new model is an update from that presented in *Folsom et al.* [2020]. The new follows a stratigraphic column with geologic units consistent with those mapped in the field [*Rhodes et al.*, 2011]. The new model recognizes a pronounced north-striking outflow path, coincident with acid sulfate alteration and pervasive silicification of sediments. This zone is channelized within beach-deposits, bar gravels and other permeable strata deposited along the shoreline of ancestral lakes in the basin. The zone is marked by a sharp gravity anomaly attributed to the densification of these sediments. Other additions to the model include updated fault geometries and inclusion of a Tertiary claystone unit that marks the bottom of the alluvium in the field. Figure 3 shows a representative cross section.

Borehole

Borehole image logs can observe failures in the formation surrounding the well bore to constrain the magnitude and orientation of stress [e.g., *Zoback*, 2007]. As part of the North Valley Project in the San Emidio geothermal area, Ormat has drilled five new wells. Logs describing the lithology of the cuttings and circulation of the drilling mud are especially useful for characterizing the 3-dimensional structure. Wireline logging of new wells drilled in 2022 include: (a) electrical logs of porosity, density, resistivity; (b) image logs; and (c) sonic logs. To capture fractures and breakouts, the drilling team deployed a full-bore formation micro imager (FMI) tool in each of the five new boreholes. In addition, well 17A-21 has been logged using the 3D far-field sonic service (3DFFS) [e.g., *Kumar et al.,* 2019]. Rock cuttings from well 17A-21 were collected to measure density and porosity. The well logs have been interpreted in detail, as described at this meeting [*Sone et al.*, 2023].

We are also using regional indicators of stress to constrain the far-field boundary conditions, as described elsewhere [*Jahnke*, 2022; *Jahnke et al.*, 2022; *Jahnke et al.*, in review].

Geodesy

Geodesy measures deformation of the ground surface. Two continuously operating GPS stations, SEMS and SEMN, have been installed on monuments attached to idle wellheads within the geothermal field at San Emidio. A third GPS station, named GARL, is located outside the geothermal area in the mountain range to the northeast of the power plant to provide a stable reference point. We analyze the GPS data to calculate daily measurements of (relative) position coordinates in three dimensions that can be modeled as time series of displacement [*Blewitt et al.*, 2018; *Kreemer et al.*, 2020].

Interferometric Synthetic Aperture Radar (InSAR) data also measures ground deformation. We are analyzing InSAR data collected by several satellite missions. One data set consists of radar images acquired monthly beginning in 2019 by the TerraSAR-X [*Pitz and Miller*, 2010] and TanDEM-X [*Krieger et al.*, 2007] satellite missions operated by the German Space Agency (DLR). We are also analyzing InSAR data from the SENTINEL-1 satellite mission [*Salvi et al.*, 2012] operated by the European Space Agency (ESA). These data sets cover the site from late 2014 through the present. To analyze these data, we are developing two high-throughput workflows using HT-Condor [*Reinisch*, 2019]. For the TerraSAR-X and TanDEM-X data, the workflow uses the GMT-SAR processing software [*Sandwell et al.*, 2011]. For the data acquired by the SENTINEL missions, we use the Interferometric synthetic aperture radar Scientific Computing Environment (ISCE) that is being developed by colleagues at NASA's Jet Propulsion Laboratory [*ISCE*, 2020].

Hydrology

Hydrology measures pressure and temperature in multiple boreholes to quantify the propagation of fluid-pressure fronts and changes to effective normal stress. The hydrologic data set consists of pressure and temperature measurements in 13 observation wells recorded every 5 minutes from April through May 2022. Routine measurements of pressure, flow rate, and temperature at production and injection wells were also recorded.

Existing evidence from San Emidio indicates that the subsurface is highly heterogeneous. We are testing the hypothesis that the fluid-flow pathways are controlled by faults, as we inferred at Brady Hot Springs during the PoroTomo project [*Patterson*, 2018]. At San Emidio, we are using analytical and numerical models to match the histories of pressure and flow, as described at this meeting [*Cardiff et al.*, 2023].

Seismic data

Seismology can determine the locations and focal mechanisms of microseismic events. Several studies indicate that anthropogenic perturbations to hydrological systems can alter the state of stress sufficiently to trigger seismic slip on pre-existing faults [e.g., *Raleigh et al.*, 1976 ; *Ellsworth*, 2013; *Segall and Lu*, 2015]. Similarly, extracting and injecting brine out of and into geothermal fields can also induce seismicity, especially in enhanced geothermal systems (EGS) [*Majer et al.*, 2007; *Brodsky and Lajoie*, 2013; *NRC*, 2013; *Kwiatek et al.*, 2015; *McGarr et al.*, 2015; *Trugman et al.*, 2016; *Andrés et al.*, 2019; *Farkas et al.*, 2021]. Such induced seismicity is caused by changes to the state of stress in and around the geothermal reservoir. Indeed, we hypothesize that increasing pore-fluid pressure reduces the effective normal stress acting across preexisting faults and induces microseismic events.

Seismic surveys

We are analyzing seismic data acquired at San Emidio in December 2016, April 2021, and April 2022. Each seismic survey was scheduled to span a short time interval (henceforth "shutdown") when the pumping operations were temporarily stopped for maintenance at the power plant and subsequently restarted.

In 2016, an array of ~1,300 vertical-component seismic stations operated by Microseismic Inc. recorded for about a week as part of DOE entitled, "A Novel Approach to Map Permeability Using Passive Seismic Emission Tomography" [*Warren et al.*, 2019].

Seismic tomography — when combined with density models estimated from gravimetric surveys — also provides constraints on material properties such as Poisson's ratio and shear modulus. For example, Figure 4 shows a vertical cross section of P-wave velocity V_P as estimated by tomographic inversion from the seismic data collected in 2016 [*Guo et al.*, in prep]. The structure resembles the resistivity from a 3-dimensional inversion of magnetotelluric data (Figure 5)[*Folsom et al.*, 2020].

In April 2021, an array of 37 three-component seismic instruments (henceforth seismographs) was deployed near the center of the 2016 array and recorded for about four weeks as part of the WHOLESCALE project.

In 2022, the WHOLESCALE team successfully deployed 450 SmartSolo 3-component seismographs in and around the San Emidio geothermal field for four weeks. As mapped in Figure 6, the 2022 array covers most of the northern two-thirds of the 2016 array footprint at twice the instrument spacing. The plan accommodated construction work around the new (North Valley) power plant (Figure 6). In the first phase, we used Real-Time Kinematic (RTK) GPS with EMLID RS2 instruments to stake out the position for each seismic station with respect to a base station that had previously been positioned with respect to the continuously operating GPS stations SEMN and SEMS. After post-processing, the resulting coordinates for the seismic stations are precise (and presumably accurate) at the centimeter level. Then the seismographs were shipped to San Emidio from the PASSCAL Instrument Center in Socorro, New Mexico. The second phase consisted of deploying the seismographs at the staked sites. The third phase, in April, involved visiting each site to turn on the seismographs to begin recording data. During this time, we downloaded and inspected the first day's data from one seismograph. The data quality was as expected. The seismographs were turned off, removed from the ground, and cleaned on May 6th (157 sites), May 7th (157 sites), and May 8th (136 sites). After downloading the data from the seismographs in the workroom at San Emidio over two long days, we shipped the seismographs back to the PASSCAL Instrument Center.

Data quality and quantity

Following the completion of the WHOLESCALE 2022 seismic deployment, we evaluated the quantity and quality of the seismic data. We recovered raw data from all 450 of the seismographs deployed. A total of 13,913 station days of three-component short-period seismic data were recorded. This led to a total of 5.54 TB of data in the SmartSolo DLD format and 6.71 TB of data in the SAC format. One station, SmartSolo serial number 12484 (station 3115) had a hardware failure after 7.9 days and therefore only recorded data from 2022/04/05 18:13:50 to 2022/04/13 15:14:38 (UTC). The remaining 449 stations recorded data continuously from the time when they were manually started until the time when they were stopped some four weeks later. The last station was started on 2022/04/08 at 00:02:48 UTC and the first station was stopped on 2022/05/06 at 16:08:28 UTC for a total time of 28.7 days. The percentage of the data recovered between the time the last station was started until the time the first station was stopped is 99.8% of total data possible if all 450 stations had recorded the entire 28.7 days (excepting the brief time interval when one station was paused to download the first 24 hours of data recorded to verify data quality).

To evaluate if the seismic data are sufficient quality to allow for quantitative interpretation, we have visually examined the waveforms for two 1-hour time windows of the seismograms recorded on all three components at each of the seismic stations. During these intervals, no station showed a flat or non-responsive recording. Some of the seismograms recorded at stations near the road show more noise during local daylight hours than at night. We attribute this noise to construction work that was taking place in April 2022.

We consider seismograms recording two moderate-sized events located in the southwest Pacific Ocean. These events occurred before and during the shutdown in April 2022, respectively. The first event occurred at 2022/04/17 07:46:36 UTC in Vanuatu at a depth of 200 km and a magnitude of Mw 6.1. This event was recorded before the shutdown at San Emidio by 449 of the 450 seismic stations there. Figure 7 shows seismograms for 1-hour window recorded at several stations located in different parts of the San Emidio valley. The seismograms show very clear P-wave and surface-wave arrivals. The second event occurred on 2022/04/19 04:33:43 UTC, some 119 km east of 'Ohonua, Tonga at 18.5 km depth with magnitude Mw 6.1. The seismograms show clear P-wave and S-wave arrivals from the 3-component stations (Figure 8). The observed phase arrivals agree with the arrival times calculated using a 1-D reference earth model named *iasp91* [*Kennett and Engdahl*, 1991], thus providing confidence in the accuracy of station timing.

We conclude that the seismic data have sufficient signal fidelity and timing accuracy to allow quantitative analysis.

DISCUSSION

By analyzing the data streams at geothermal fields, we can take advantage of the perturbations created by pumping operations to infer temporal changes in the state of stress in the geothermal system. For example, the PoroTomo experiment was conducted at the geothermal field at Brady Hot Springs, Nevada [*Feigl and Parker*, 2019]. There, a scheduled cessation of both production and injection pumping produced fluid pressure changes as large as 150 kPa (roughly equivalent to 15 m of water) [*Patterson et al.*, 2017] that are associated with microseismic events with magnitude less than M 2 [*Cardiff et al.*, 2018]. At Brady, these authors observed that "shutdowns in pumping for plant maintenance correlate with increased microseismicity" [*Cardiff et al.*, 2018]. Following these authors, we hypothesize that "extraction of fluids inhibits fault slip by increasing the effective [normal] stress on faults; in contrast, brief pumping cessations represent times when effective [normal] stress is decreased below its long-term average, increasing the likelihood of microseismicity" [*Cardiff et al.*, 2018].

Similar phenomena have been observed at San Emidio. In the month of December 2016, more than 100 discrete microseismic events were detected as the power plant and pumping were shut down for maintenance and subsequently restarted [*Warren et al.*, 2018; *Warren et al.*, 2019]. These microseismic events are small in magnitude. Although they can be detected by sensitive seismic instruments, they were not — and cannot be — felt by humans. Recent work indicates that the discrete events detected in December 2016 have a maximum (coda) magnitude M_c less than zero [*Guo et al.*, in prep].

Magnitude of seismicity

Following *Feigl et al.* [2022], we evaluate the microseismic events around San Emidio by considering catalogs of events compiled from seismic data recorded by the U.S. Geological Survey [*USGS*]. Considering the 22-year time interval between January 1st, 2013 and December 31st, 2022 and the region within a 5–km radius of the power plant at San Emidio, the USGS catalog contains only one event with magnitude greater than 3; it was located 24 km south of Empire, Nevada on 2005-07-03 at 07:58:09.480 UTC with local m_L magnitude of 3.4. Considering the same 22-year time interval and 5-km radius, the USGS catalog contains only five events with local magnitude $2.0 \leq m_L \leq 2.9$.

To estimate the magnitude of the microseismic events detected in December 2016, April 2021, and April 2022 by the temporary, local seismic networks around San Emidio, we combine two observations in a logical syllogism. First, we note that the USGS catalog does not include any events located within 10 km of the power plant at San Emidio during any of the three time intervals: December 2016, April 2021, or April 2022. Second, we note that during the time interval between January 1st, 2013 and December 31st, 2020, the magnitude of completeness of the USGS catalog is M 1.3. To determine this value, we have examined Gutenberg-Richter plots for the comprehensive (de-clustered) seismicity catalog "ComCat". [USGS, 2017]. Considering a sample of n = 100 events nearest (< 42 km from) the power plant at San Emidio, we find that the curve showing the logarithm of the cumulative number of events below a given magnitude begins to deviate from a straight line at M 1.3. Considering a sample of n = 200 events nearest (< 80 km from) the power plant at San Emidio, we also find a completeness magnitude of M 1.3. By combining the two observations, we infer that the events detected by the local, temporary seismic networks have magnitudes less than M 1.3.

We are now creating a catalog of microseismic events for the 2016, 2021, and 2022 datasets. To do so, we use the REST workflow by Steve Roecker [*Lanza et al.*, 2019] to perform automatic phase detection, iterative onset estimation, phase association, and preliminary event location. We used the same parameters in processing the 2016, 2021, and 2022 data so that relatively unbiased comparisons between the three shutdown periods can be made. We used the same subset of 51 stations spaced at ~300 to ~400 meters (covering the northern two thirds of the 2016 deployment area) for processing the 2016 and 2022 datasets, and all 37 stations for processing the 2021 dataset. The latter set of stations overlaps the southern part of the 51-station subsets used for 2016 and 2022.

For each of the three years, we have processed data from the day of the shutdown and the following day. We focused on determining the appropriate REST parameters for earthquake detection, allowing the maximum number of events to be detected while minimizing the number of false positives. This produced preliminary catalogs with 28 events on the UTC day of the shutdown and 610 events on the following day in 2016, 455 events on the shutdown day and 868 events on the following day in 2021, and 170 events on shutdown day and 821 events on the following day in 2022. As shown in Figure 9, the average number of events per hour is markedly higher during each shutdown than before it. We hypothesize that the events are related to the geothermal brine recovering during shutdown.

The preliminary results show very different spatial distributions for the events. The 2016 events were concentrated beneath the northern part of the array where the then-primary production wells were situated. The 2021 events were located along the northwest edge of the 2021 array, near a new production well. The 2022 events were located between the 2016 and 2022 events.

In February 2022, i.e. before the seismic survey in April 2022, we documented our expectations for the shutdown in April 2022 as follows [*Feigl et al.*, 2022].

> *"The operators of the power plant are planning to suspend normal operations for several days in April 2022. During this time interval, pumping will cease at all production and injection wells. We expect microseismic events to occur in a manner like that observed in December 2016. Specifically, Table 1 lists the variables describing microseismic events during temporary shutdowns at San Emidio, as observed in December 2016* ***and expected in April 2022.****"*

The upper and lower bounds for timing, location, elevation, and magnitude of microseismic events appear in Table 1. The values observed in 2016 appear in the 2nd and 3rd columns as they were published at the Stanford Geothermal Workshop in February 2022 [*Feigl et al.*,

2022]. The statistics observed from the preliminary analysis of the 2022 data set are listed in the 4th and 5th columns. In both cases, most of the microseismic events occurred less than 12 hours after all pumping was temporarily suspended. The interquartile ranges of ($t - t_{shutdown}$) ∈ [7.4, 12.1] hours in 2016 and ($t - t_{shutdown}$) ∈ [6.5, 11.4] hours in 2022 agree very well. This result is shown graphically in a "box-and-whisker" plot (Figure 10). This type of plot shows the median value as a red bar and the interquartile range as a blue box. The green "whiskers" delimit an interval three times larger than the interquartile range. Values outside these limits are considered outliers and plotted as magenta dots.

For the vertical location, expressed as elevation above mean sea level (i.e. orthometric height H), the interquartile ranges overlap: $H \in [588, 794]$ m in 2016 versus $H \in [-362, 950]$ m in 2022 but the median values differ at the level of 5% significance [*Mathworks*, 2021]. The preliminary locations for 2022 estimated using the REST methodology show considerable scatter, such that the horizontal distance R from each event to the nearest well varies over an interquartile range $R \in [559, 1225]$ m. This range differs significantly from the interquartile range of $R \in [243, 395]$ m for the events in 2016 relocated with a precise methodology.

At San Emidio, the location and timing of the events in December 2016 are consistent with time-dependent 3-dimensional numerical models that show increased fluid pressure over length scales of the order of several kilometers from the production wells and temporal scales of the order of tens of hours from the cessation of production and injection, as described at this meeting [*Cardiff et al.*, 2023].

CONCLUSIONS

Tomographic models of seismic velocity and resistivity show contrasts that are consistent with normal faults striking north-south and dipping westward. The locations of microseismic events have been determined from seismic data recorded by a local seismic network in 2016. Many of the events appear to occur on or near normal faulting structures in the geologic model. The focal mechanisms of microseismic events have also been determined from seismic data recorded by a local seismic network in 2016. Several of the events cluster on a plane dipping westward. The focal mechanisms are consistent with a normal-faulting regime with the maximum horizontal stress oriented approximately North-South.

The field experiment in 2022 collected data from seismology, drilling, geology, geodesy, and hydrology. By analyzing these data, we are working to constrain models for simulating the stress, strain, pressure, and temperature in the geothermal system using an open-source, numerical simulator named GEOSX.

ACKNOWLEDGMENTS

The WHOLESCALE team thanks the following individuals at Ormat: Curtis Peach, Cliff Reed, Joe Pavone, Manolo Di Donato, Leeta Miller, Alan Pinuelas-Molina, David Schwab, Lupé Gonsalez Ortiz, Gabrielle Ramirez, Courtney Brailo, Zack Young, John Murphy, and Robin Zuza. We also acknowledge the data shared by Ormat Technologies, Inc.

We also thank all the individuals who contributed to the field work: DJ Bustos (PASSCAL), Alan Horton (PASSCAL), Ben Heath (UW-Madison), Peter Sobol (UW-Madison), Sabrina Bradshaw (UW-Madison), Samantha Kleich (UW-Madison), Anya Wolterman (UW-Madison), Ben Jahnke (UW-Madison), Zirou Jin (UW-Madison), Nina Miller (UNR), and Bret Pecoraro (UNR).

Some of the figures in this paper were generated using Leapfrog Geothermal Software Leapfrog (Bentley Systems, Incorporated).

Passive seismic data collections were completed at San Emidio in late 2016 by Microseismic Inc. as part of DOE project number DE-EE0007698 as described at https://gdr.openei.org/submissions/1386

For the 2022 survey, seismic instruments were provided by the Incorporated Research Institutions for Seismology (IRIS) through the PASSCAL Instrument Center at New Mexico Tech. Data collected will be available through the IRIS Data Management Center. The facilities of the IRIS Consortium are supported by the National Science Foundation's Seismological Facilities for the Advancement of Geoscience (SAGE) Award under Cooperative Support Agreement EAR-1851048.

The work presented herein has been funded in part by the Office of Energy Efficiency and Renewable Energy (EERE), U.S. Department of Energy, under Award Numbers DE-EE0007698 and DE-EE0009032.

Table 1. Variables describing microseismic events during temporary shutdowns at San Emidio, events observed in December 2016 (as published previously [*Feigl et al.*, 2022]) and April 2022 (as estimated via RESTT [*Thurber et al.*, 2022])

Variable	Lower bound (2016)	Upper bound (2016)	Lower bound (2022)	Upper bound (2022)	Notes
Timing: hours after cessation of production and injection.	7.4 hours	12.1 hours	6.5 hours	11.4 hours	Bounds represent 25th and 75th percentiles, respectively. Seismic data were recorded only for ~40 hours following resumption of production in 2016. For 2022, only 48 hours of data have been analyzed.
Location (radial distance from nearest production well)	243 m	395 m	559 m	1225 m	Bounds represent 25th and 75th percentiles, respectively. Locations for 2022 are preliminary.
Elevation above WGS84 geoid	588 m	794 m	–362 m	950 m	Bounds represent 25th and 75th percentiles, respectively.
Magnitude	Not defined	M 1.3	Not defined	M 1.3	Completeness magnitude of catalog.

FIGURES

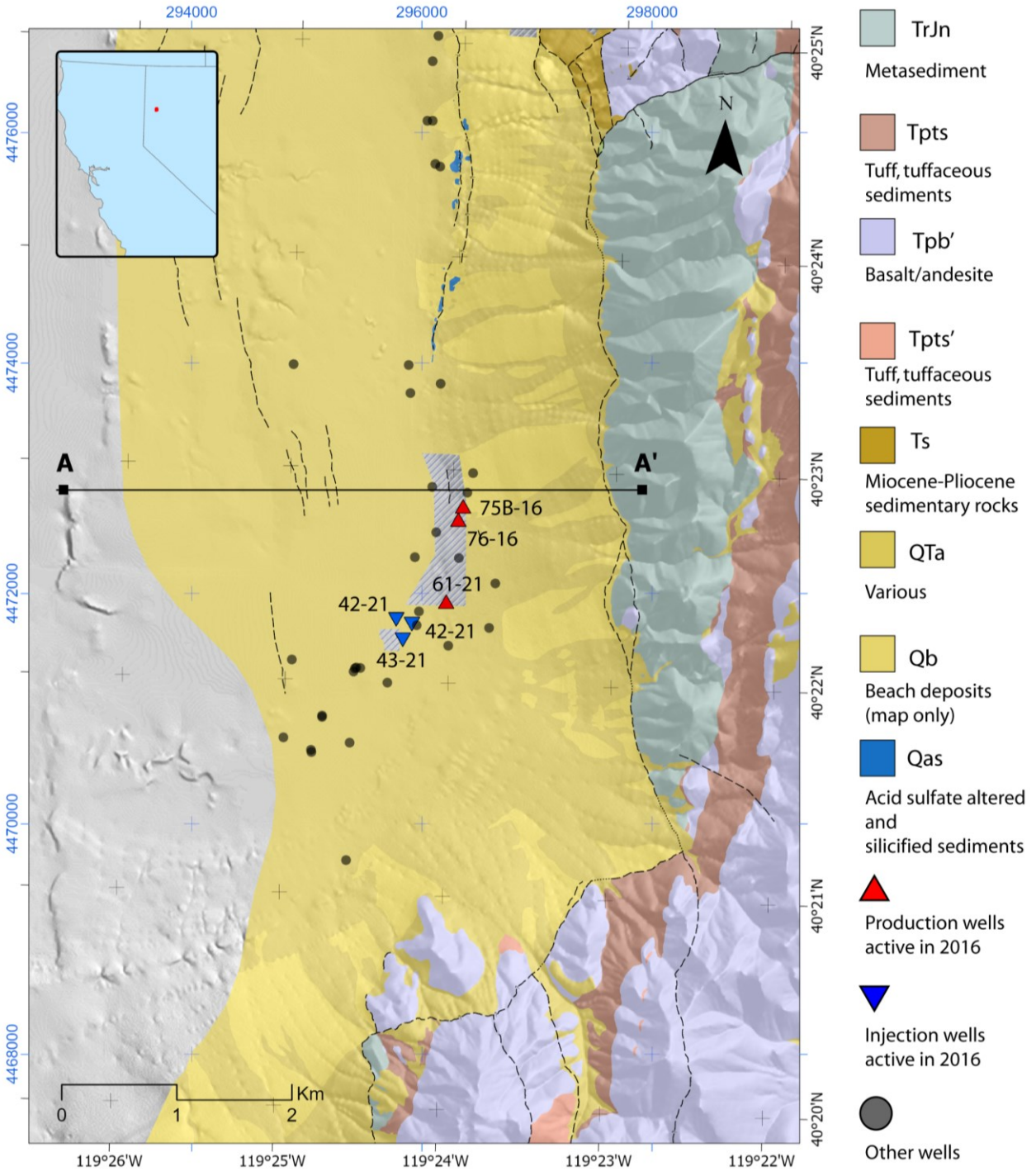

Figure 1: Map of the WHOLESCALE study area at San Emidio, showing geologic model simplified from mapping [*Rhodes et al.*, 2011]. Black tick marks and labels on the east and south edges give geographic (WGS84) latitude and longitude, respectively in degrees and minutes. Blue ticks and labels on north and west edges give easting and northing coordinates, respectively, in meters in Zone 11 of the Universal Transverse Mercator (UTM) projection.

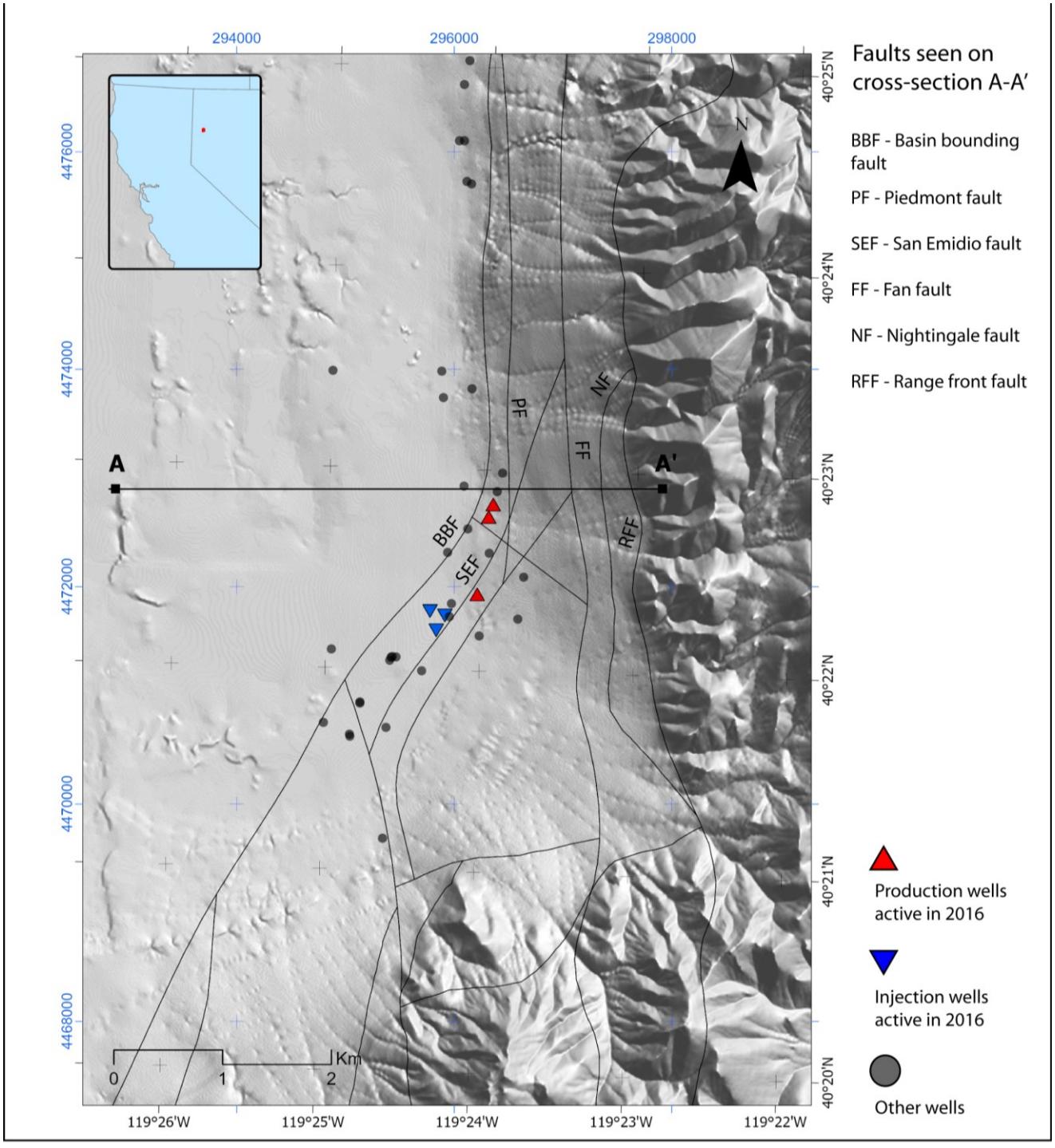

Figure 2: Map of the WHOLESCALE study area at San Emidio, showing surface traces of faults in a geologic model updated by Matt Folsom in 2022. Faults include: Basin-bounding fault (BBF), San Emidio Fault (SRF), Piedmont Fault (PF), Nightingale Fault (NF), and Range Front Fault (RFF). Black tick marks and labels on the east and south edges give geographic (WGS84) latitude and longitude, respectively in degrees and minutes. Blue ticks and labels on north and west edges give easting and northing coordinates, respectively, in meters in Zone 11 of the Universal Transverse Mercator (UTM) projection.

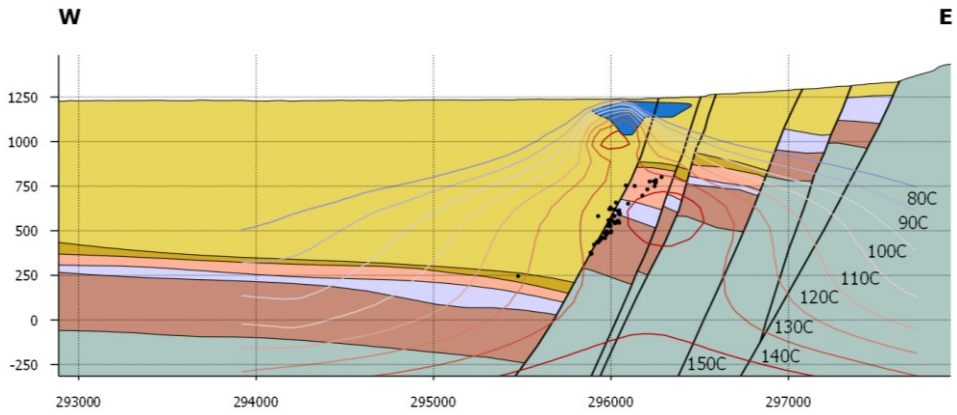

Figure 3. Geologic cross section, showing primary lithologic units, wells, and faults, as recently updated by Matt Folsom from previous studies [*Rhodes*, 2011; *Rhodes et al.*, 2011; *Folsom et al.*, 2020; *Folsom et al.*, 2021] Vertical plane is an E-W transect at UTM Northing coordinate 472,900 m between points A and A' shown on maps (Figure 1 and Figure 2). Color codes denote geologic units as in Figure 1. Contours show "natural state" temperature in degrees Celsius. Faults (black lines) and relocated microseismic events (black dots) have been projected from 200 m onto the vertical plane. Most of the hypocenters are located between the San Emidio Fault (SEF) and the Basin Bounding Fault (BBF). Horizontal axis shows Easting coordinate in meters. Vertical coordinate axis shows elevation above mean sea level (WGS 84 geoid) in meters.

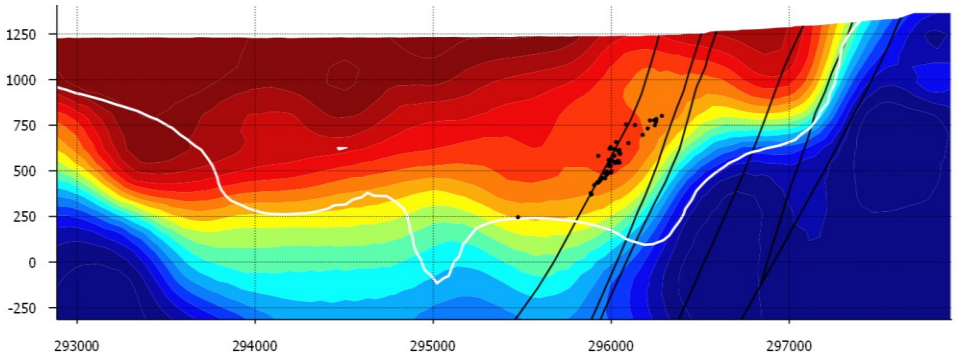

Figure 4. Seismic cross section, showing P-wave velocity in km/s (colors) and microseismic events (black circles) [*Guo et al.*, in prep]. Seismic data from 2016 survey [*Warren et al.*, 2018; *Warren et al.*, 2019]. Color scale ranges less than 2000 m/s (dark red) to greater than 5400 m/s (dark blue). White contour delineates resolvability of 0.62. Plotting conventions as in previous figure.

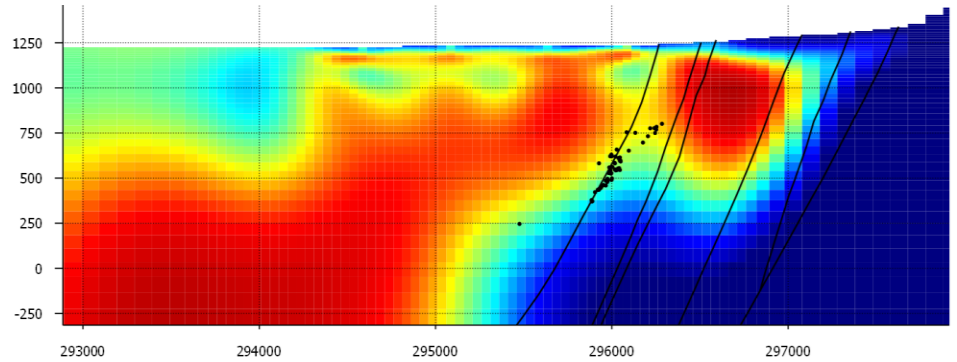

Figure 5. Resistivity estimated by 3-D inversion of magnetotelluric data [*Folsom et al.*, 2020; *Folsom et al.*, 2021]. Resistivity values range from 1 Ω·m (red) to 100 Ω·m (blue). Vertical plane is an E-W transect at Northing coordinate 472,900 m. Faults (black lines) and microseismic events (black dots) have been projected from 200 m onto the vertical plane. Plotting conventions as in previous figure.

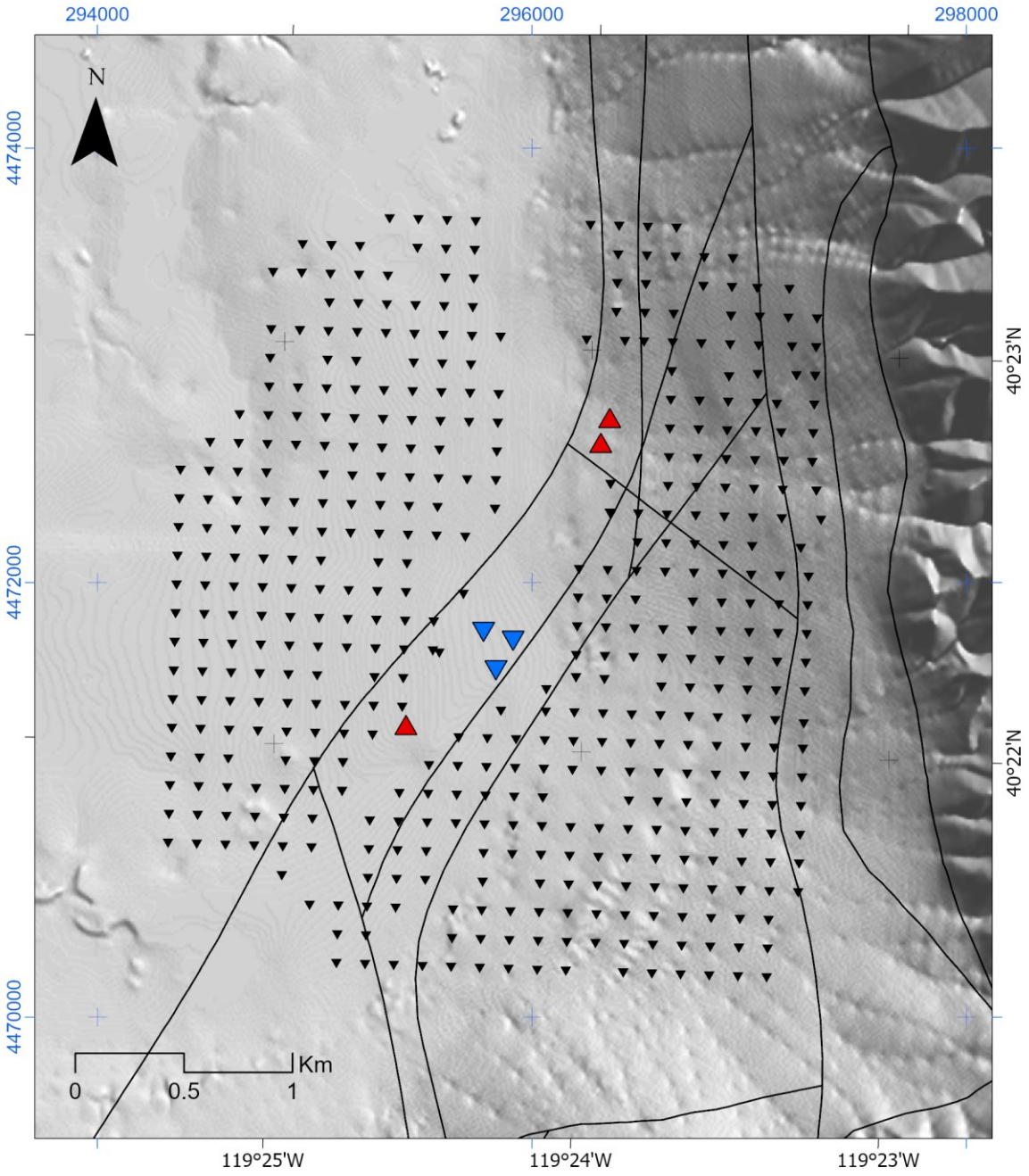

Figure 6 Map of seismic stations (black triangles) deployed in April 2022, showing production wells (red triangles) and injection wells (blue triangles). The gap running roughly north-south through the area accommodates roads and pipeline construction.

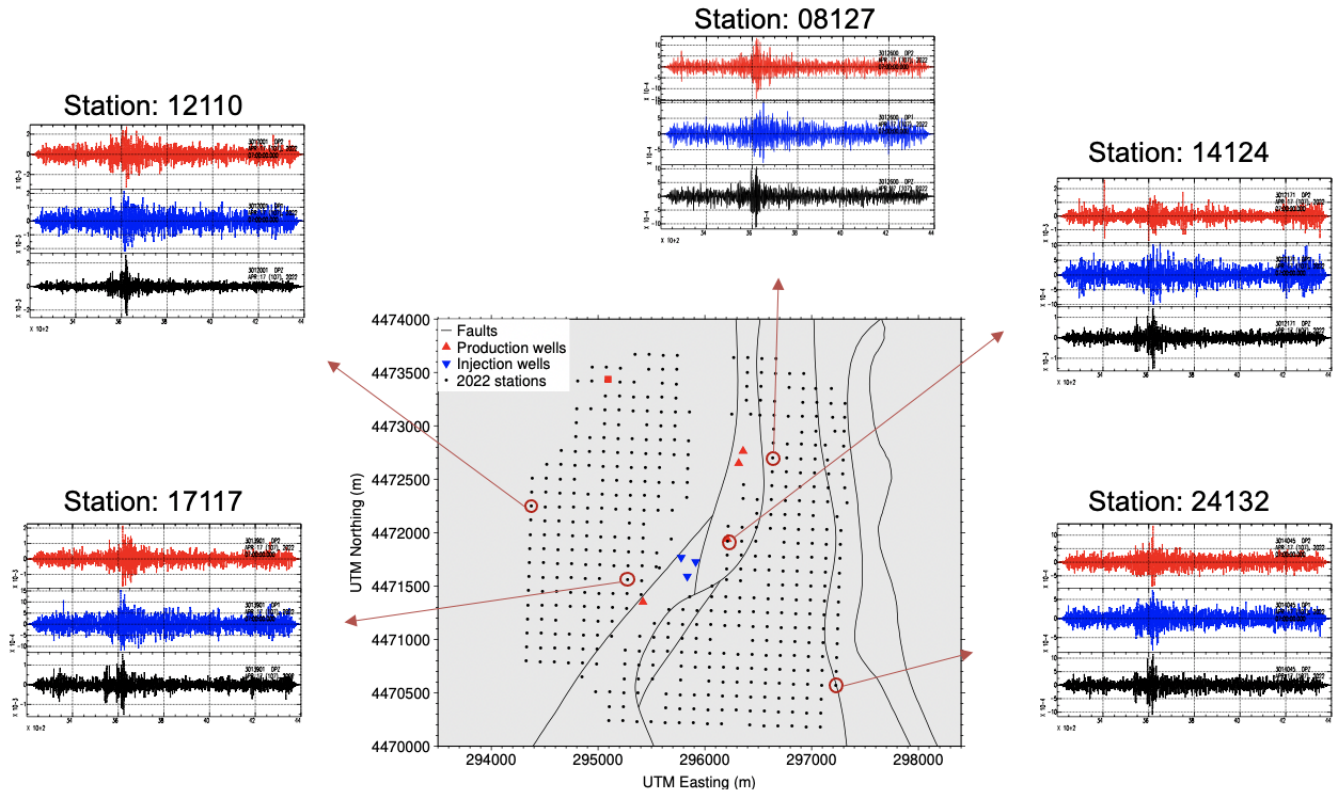

Figure 7. Example seismograms showing a teleseismic event on 17 April 2022 UTC, i.e., before the plant shutdown. Horizontal axes show time in hundreds of seconds.

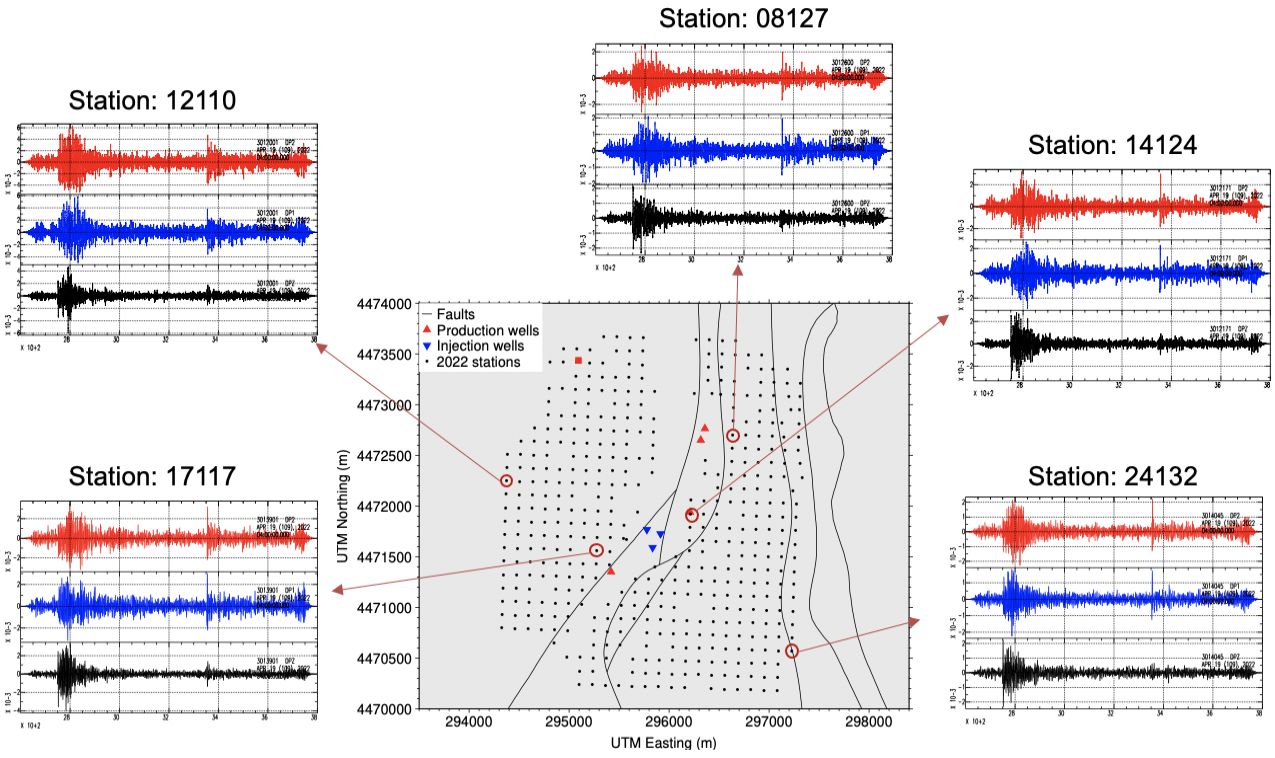

Figure 8 Example seismograms showing a teleseismic event on 19 April 2022 UTC, i.e. during the plant shutdown. Horizontal axes show time in hundreds of seconds.

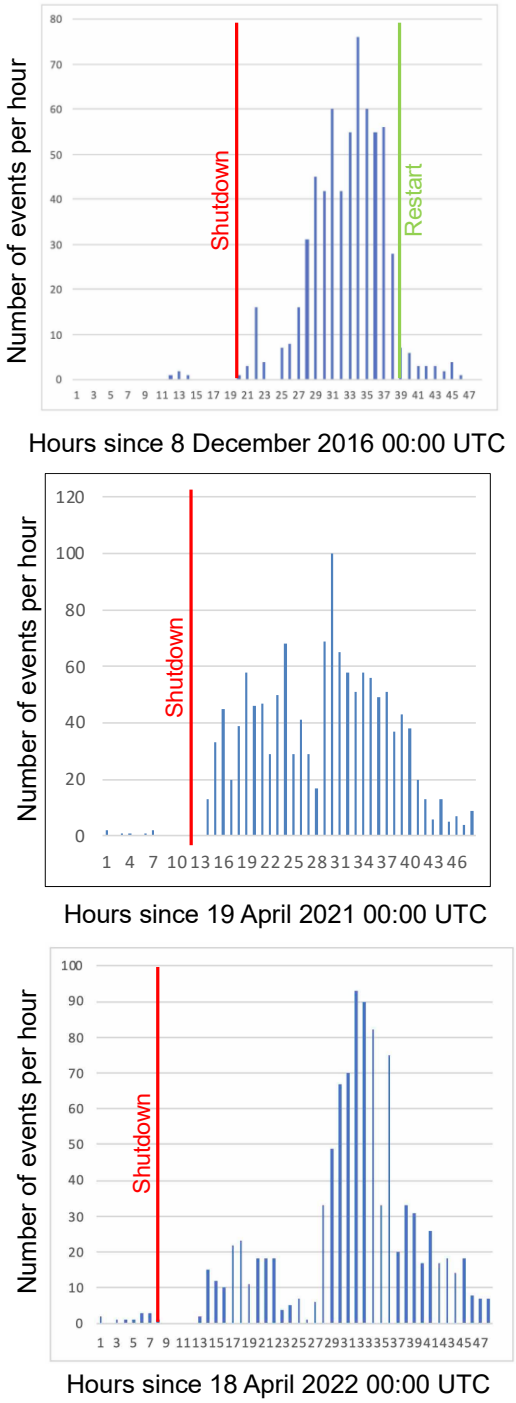

Figure 9. Timelines of microseismic events detected at San Emidio for 48-hour intervals in December 2016 (top), April 2021 (middle), and April 2022 (bottom) . Most of the detected events occurred during the plant shutdowns when the power plant was shut down and all pumping was intentionally and temporarily paused.

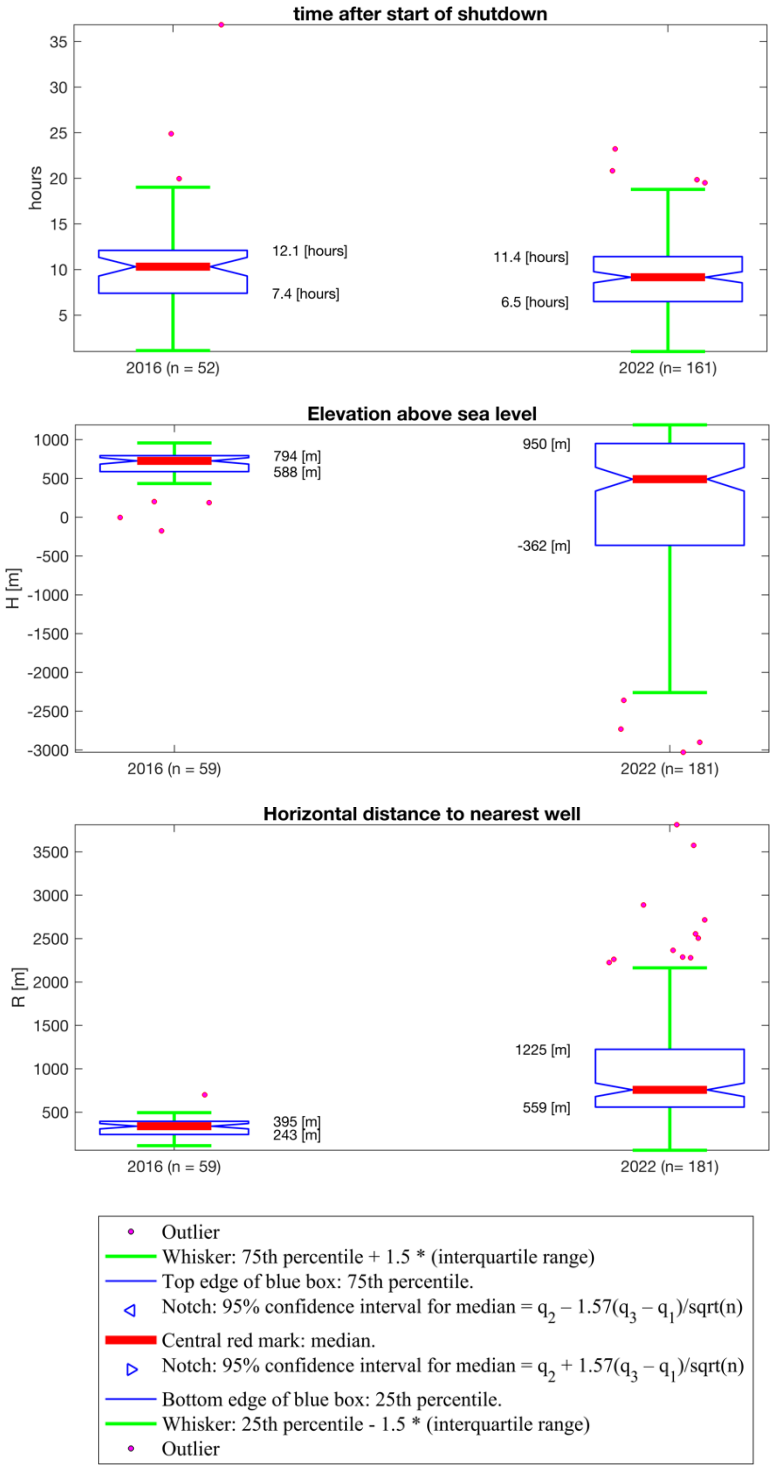

Figure 10. Distributions of characteristics of microseismic events observed in December 2016 (relocated by *Thurber et al.* [2021] and reported by *Feigl et al.* [2022]) and April 2022 (as estimated automatically via RESTful [*Thurber et al.*, 2022]), showing time after the start of the shutdown (top panel), elevation *H* above mean sea level (2nd panel), and distance *R* to nearest well (3rd panel). The 2016 shutdown began on 2016/12/08 at 19:32 UTC. Events before this time are not shown in the left side of upper panel. The 2022 shutdown began on 2022/04/18 at 23:31 UTC. Only events with preliminary locations estimated automatically that fall below the ground surface are shown for 2022.The lower panel shows a legend for these "box and whisker" plots. The central red mark denotes the median. The bottom and top edges of each blue box delimit the interquartile range, labeled with the 25th and 75th percentiles, respectively. The notches in the blue box delimit the 95% confidence interval for the median. The green "whiskers" delimit the interval delimited by the 3 times the interquartile range. Data points outside the green whiskers show outliers as magenta circles. Box plots made with MATLAB function *boxplot* [*Mathworks*, 2021].

REFERENCES

Andrés, S., D. Santillán, J. C. Mosquera, and L. Cueto-Felgueroso (2019), Thermo-Poroelastic Analysis of Induced Seismicity at the Basel Enhanced Geothermal System, Sustainability, 11. http://dx.doi.org/10.3390/su11246904

Blewitt, G., W. C. Hammond, and C. Kreemer (2018), Harnessing the GPS Data Explosion for Interdisciplinary Science, Eos, 99. https://doi.org/10.1029/2018EO104623

Brodsky, E. E., and L. J. Lajoie (2013), Anthropogenic Seismicity Rates and Operational Parameters at the Salton Sea Geothermal Field, Science. http://dx.doi.org/10.1126/science.1239213

Cardiff, M., D. D. Lim, J. R. Patterson, J. Akerley, P. Spielman, J. Lopeman, . . . K. L. Feigl (2018), Geothermal production and reduced seismicity: Correlation and proposed mechanism, Earth and Planetary Science Letters, 482, 470-477. https://doi.org/10.1016/j.epsl.2017.11.037

Cardiff, M., C. Sherman, H. Guo, E. Cunningham, M. Folsom, I. Warren, . . . K. L. Feigl (2023), WHOLESCALE - Calibration and Simulation of hydro-mechanical Behavior at San Emidio, Nevada During Operational Changes, paper presented at Stanford Geothermal Workshop, Stanford, California.

Ellsworth, W. L. (2013), Injection-induced earthquakes, Science, 341, 1225942. http://www.ncbi.nlm.nih.gov/pubmed/23846903

Eneva, M., G. Falorni, W. Teplow, J. Morgan, G. Rhodes, and D. Adams (2011), Surface Deformation at the San Emidio Geothermal Field, Nevada, from Satellite Radar Interferometry, GRC Transactions, 35.

Farkas, M. P., H. Hofmann, G. Zimmermann, A. Zang, F. Bethmann, P. Meier, . . . N. Josephson (2021), Hydromechanical analysis of the second hydraulic stimulation in well PX-1 at the Pohang fractured geothermal reservoir, South Korea, Geothermics, 89.

Faulds, J. E. (2014), 3D Model of the San Emidio Geothermal Area [data set], Geothermal Data Repository. https://gdr.openei.org/submissions/365.

Feigl, K. L., and L. M. Parker (2019), PoroTomo Final Technical Report: Poroelastic Tomography by Adjoint Inverse Modeling of Data from Seismology, Geodesy, and Hydrology, Medium: ED; Size: 176 p. pp, ; Univ. of Wisconsin, Madison, WI (United States). https://www.osti.gov/servlets/purl/1499141

Feigl, K. L., E. C. Reinisch, S. A. Batzli, H. Sone, M. A. Cardiff, J. C. Hampton, . . . C. Sherman (2020), Spatio–Temporal Analysis of Deformation at San Emidio Geothermal Field, Nevada, USA between 1992 and 2010, paper presented at Proceedings 45th Workshop on Geothermal Reservoir Engineering Stanford University, Stanford, California, February 10-12, 2020 https://pangea.stanford.edu/ERE/db/GeoConf/papers/SGW/2020/Feigl.pdf

Feigl, K. L., S. Tung, H. Guo, E. Cunningham, J. Hampton, S. J. Kleich, . . . H. F. Wang (2022), Overview and Preliminary Results from the WHOLESCALE project at San Emidio, Nevada, U.S., paper presented at 47th Workshop on Geothermal Reservoir Engineering, Stanford, California. https://pangea.stanford.edu/ERE/pdf/IGAstandard/SGW/2022/Feigl.pdf

Folsom, M., R. Libbey, D. Feucht, W. I., and S. Garanzini (2020), Geophysical Observations and Integrated Conceptual Models of the San Emidio Geothermal Field, Nevada. , paper presented at Workshop on Geothermal Reservoir Engineering, Stanford, California, USA. https://pangea.stanford.edu/ERE/db/GeoConf/papers/SGW/2020/Folsom.pdf

Folsom, M., R. Libbey, D. Feucht, I. Warren, and S. Garanzini (2021), Geophysical observations and integrated conceptual models of the San Emidio Geothermal Field, Nevada, paper presented at Nevada Petroleum & Geothermal Society, February 4th, 2021.

Guo, H., C. H. Thurber, B. A. Heath, M. Cardiff, N. Lord, I. Warren, and K. L. Feigl (2022 of Conference), Seismic analysis of reservoir conditions for inducing seismicity at the San Emidio geothermal field, Nevada, U.S.A., abstract presented at Annual Meeting Seismological Society of America, Bellevue, WA, USA, 19-23 April 2022.

Guo, H., C. Thurber, I. Warren, B. Heath, M. Folsom, N. Lord, and K. L. Feigl (in prep), Seismic Analysis of Induced Microseismicity due to Pumping Cessation at the San Emidio Geothermal Field, Nevada.

Jahnke, B. (2022), Geomechanical Analysis of the Geothermal Reservoir at San Emidio, Nevada and Fracture Toughness Anisotropy of EGS Collab Testbed Rocks, M.S. thesis thesis, University of Wisconsin-Madison (H. Sone, advisor).

Jahnke, B., H. Guo, B. Heath, E. Cunningham, C. Sherman, H. Sone, . . . WHOLESCALE_Team (2022), Spatial-Temporal Stress Heterogeneity in the Geothermal Reservoir at San Emidio, Nevada, U.S., paper presented at 45th Workshop on Geothermal Reservoir Engineering, February 7-9, 2022, Stanford University, Stanford, California,.

Jahnke, B., H. Sone, H. Guo, C. Sherman, I. Warren, C. Kreemer, . . . WHOLESCALE_Team (in review), Geomechanical Analysis of the Geothermal Reservoir at San Emidio, Nevada, Geothermics.

Kennett, B. L. N., and E. R. Engdahl (1991), Traveltimes for global earthquake location and phase identification, Geophysical Journal International, 105, 429-465. https://doi.org/10.1111/j.1365-246X.1991.tb06724.x

Kreemer, C., G. Blewitt, and P. Davis (2020), Geodetic evidence for a buoyant mantle plume beneath the Eifel volcanic area, NW Europe, Geophysical Journal International, 222., 1316-1332. https://doi.org/10.1093/gji/ggaa227

Kwiatek, G., P. Martínez-Garzón, G. Dresen, M. Bohnhoff, H. Sone, and C. Hartline (2015), Effects of long-term fluid injection on induced seismicity parameters and maximum magnitude in northwestern part of The Geysers geothermal field, Journal of Geophysical Research: Solid Earth, 120, 7085-7101. https://agupubs.onlinelibrary.wiley.com/doi/abs/10.1002/2015JB012362

Kumar, Rajeev, Nicholas Bennett, Adam Donald, Gabriela Martinez, and Edgar Velez. "3d Borehole Sonic Imaging for Input to Structural Modeling-a Quantitative Approach." Paper presented at the SPE Middle East Oil and Gas Show and Conference, 2019. https://doi.org/10.2118/194810-MS

Lanza, F., C. J. Chamberlain, K. Jacobs, E. Warren-Smith, H. J. Godfrey, M. Kortink, . . . D. Eberhart-Phillips (2019), Crustal Fault Connectivity of the Mw7.8 2016 Kaikōura Earthquake Constrained by Aftershock Relocations, Geophysical Research Letters, 46, 6487-6496.

Lund, J. W., and P. J. Lienau (1994), Onion and Garlic Dehydration in the San Emidio Desert, Nevada, Geo-Heat Center Quarterly Bulletin, Vol. 15, No.4. http://digitallib.oit.edu/digital/api/collection/geoheat/id/11104/download

Majer, E. L., R. Baria, M. Stark, S. Oates, J. Bommer, B. Smith, and H. Asanuma (2007), Induced seismicity associated with enhanced geothermal systems, Geothermics, 36, 185-222.

Mathworks (2021), MATLAB release 2021b documentation: boxplot - visualize summary statistics with box plot https://www.mathworks.com/help/stats/boxplot.html

Matlick, J. S. (1995), San Emidio Geothermal System, Empire, Nevada: GRC Field Trip ~ October 1995, Mesquite Group, Inc., Fullerton, California. https://data.nbmg.unr.edu/public/Geothermal/GreyLiterature/Matlick_SanEmidioGeoSystem_1995.pdf

McGarr, A., B. Bekins, N. Burkardt, J. Dewey, P. Earle, W. Ellsworth, . . . A. Sheehan (2015), Coping with earthquakes induced by fluid injection, Science, 347, 830-831. http://www.sciencemag.org/content/347/6224/830.full.pdf

Moeck, I. (2011), Stress Inversion and 2D fault stress modeling San Emidio: Project Report to PI Teplow, 19 page pp.

NRC (2013), Induced Seismicity Potential in Energy Technologies, National Acad. Press, Washington, D. C.

Patterson, J. R., M. Cardiff, T. Coleman, H. Wang, K. L. Feigl, J. Akerley, and P. Spielman (2017), Geothermal reservoir characterization using distributed temperature sensing at Brady Geothermal Field, Nevada, The Leading Edge, 36, 1024a1021 - 1024a1027. http://dx.doi.org/10.1190/tle36121024a1.1

Raleigh, C. B., J. H. Healy, and J. D. Bredehoeft (1976), An experiment in earthquake control at rangely, colorado, Science, 191, 1230-1237. http://www.ncbi.nlm.nih.gov/pubmed/17737698

Reinisch, E. C., M. Cardiff, J. Akerley, I. Warren, and K. L. Feigl (2019), Spatio–Temporal Analysis of Deformation at San Emidio Geothermal Field, Nevada, USA Between 1992 and 2010, Remote Sensing, 11, 1935. http://dx.doi.org/10.3390/rs11161935

Rhodes, G. T., J. E. Faulds, and W. Teplow (2010), Structural Controls of the San Emidio Desert Geothermal Field, Northwestern Nevada, paper presented at Geothermal Resource Council Transactions.

Rhodes, G. T. (2011), Structural controls of the San Emidio Geothermal System, M.S. thesis, vi, 73 leaves pp, University of Nevada Reno advisor).

Rhodes, G. T., J. E. Faulds, and A. R. Ramelli (2011), Preliminary Geologic Map of the Northern Lake Range, San Emidio Geothermal Area, Washoe County, Nevada, Nevada Bureau of Mines and Geology. http://data.nbmg.unr.edu/public/freedownloads/of/of2011-11.zip

Segall, P., and S. Lu (2015), Injection-induced seismicity: Poroelastic and earthquake nucleation effects, Journal of Geophysical Research: Solid Earth, 120, 5082-5103. http://dx.doi.org/10.1002/2015jb012060

Sone, H., Z. Jin, O. Mudatsir, I. Warren, M. Folsom, and K. L. Feigl (2023), WHOLESCALE - Characterization of Conductive Fractured Zones Based on Borehole Data at San Emidio Geothermal Field, Nevada, paper presented at Stanford Geothermal Workshop.

Thurber, C., H. Guo, B. Heath, M. Cardiff, N. Lord, I. Warren, and K. Feigl (2021a), Structure and Stress Results from Nodal Seismic Array Deployments at the San Emidio Geothermal Field, Nevada, USA, paper presented at AGU Fall Meeting Abstracts.

Thurber, C. H., H. Guo, B. A. Heath, M. Cardiff, N. Lord, I. Warren, and K. L. Feigl (2021b of Conference), Structure and Stress Results from Nodal Seismic Array Deployments at the San Emidio Geothermal Field, Nevada, U.S.A., abstract presented at AGU Fall Meeting, New Orleans. https://agu.confex.com/agu/fm21/meetingapp.cgi/Paper/912296

Thurber, C. H., H. Guo, E. Cunningham, B. Heath, N. E. Lord, and K. L. Feigl (2022 of Conference), Microseismic Activity During Three Shutdowns of the San Emidio Geothermal Plant, Nevada (S32B-05), abstract presented at AGU Fall Meeting, Chicago. https://agu.confex.com/agu/fm22/meetingapp.cgi/Paper/1123308

Trugman, D. T., P. M. Shearer, A. A. Borsa, and Y. Fialko (2016), A comparison of long-term changes in seismicity at The Geysers, Salton Sea, and Coso geothermal fields, Journal of Geophysical Research: Solid Earth, 121, 225-247. http://dx.doi.org/10.1002/2015jb012510

UNR (2014), Slip and Dilation Tendency Analysis of the San Emidio Geothermal Area [data set]. https://gdr.openei.org/submissions/371

USGS USGS Earthquake Hazards Program: Search Catalog. https://earthquake.usgs.gov/earthquakes/search/

Warren, I. (2010), Three-Component Long Offset Surface Seismic Survey Data Used to Find Large Aperture Fractures in Geothermal Resources - San Emidio Geothermal Resource Area, U.S. Geothermal Inc. https://doi.org/10.15121/1422726

Warren, I., E. Gasperikova, S. Pullammanappallil, S. S, and M. Grealy (2018), Mapping Geothermal Permeability Using Passive Seismic Emission Tomography Constrained by Cooperative Inversion of Active Seismic and Electromagnetic Data, paper presented at Proceedings, 43rd Workshop on Geothermal Reservoir Engineering Stanford University, Stanford, California, 2018 SGP-TR-213, February 12-14, 2018. https://pangea.stanford.edu/ERE/pdf/IGAstandard/SGW/2018/Warren.pdf

Warren, I., E. Gasperikova, and S. Pullammanappallil (2019), Final Phase 1 Report DE-EE0007698: A Novel Approach to Map Permeability Using Passive Seismic Emission Tomography. https://subterraseis.com/wp-content/uploads/2019/10/Doc1.pdf